Available online at www.sciencedirect.com
SCIENCE DIRECT
Journal of Computational Physics 213 (2006) 803–822
JOURNAL OF COMPUTATIONAL PHYSICS
www.elsevier.com/locate/jcp

Two-dimensional SPH simulations of wedge water entries

G. Oger *, M. Doring, B. Alessandrini, P. Ferrant

Fluid Mechanics Laboratory (CNRS UMR6598), Ecole Centrale de Nantes, 1, rue de la Noe, 44321 Nantes, France

Received 21 March 2005; received in revised form 20 July 2005; accepted 2 September 2005
Available online 26 October 2005

Abstract

This paper presents a study based on the smoothed particles hydrodynamics (SPH) method, aiming at an accurate numerical simulation of solid–fluid coupling in a free surface flow context. The SPH scheme is first described and discussed through its formulations. Then a new technic based on a particle sampling method, and designed to evaluate fluid pressure on solid boundaries is introduced. This method is then extended to the capture of freely moving body dynamics in a fluid/solid coupling approach. This study involves a spatially varying resolution, based on the so-called variable smoothing length technique, for which a new formulation of the equations is proposed. Two distinct test cases of wedge water entry are presented in order to validate this new method. Pressure prediction is first compared with analytical and experimental results, evolution in time of the body dynamics is compared with experimental results in both cases, and the pressure field on the solid boundaries is studied and discussed on the first impact case.

Keywords: Water entry; SPH; Pressure load evaluation; Free rigid body–fluid couplings

1. Introduction

Since the first studies by von Karman (1929) and Wagner (1932), lots of works have been carried out in slamming force prediction problems. Actually, water entry of a solid through the free surface is a persisting field of research in ship hydrodynamics applications. In deed, the knowledge of pressure forces acting locally on structures is necessary to ensure the verification of safety criteria in their design and operation. This paper presents a numerical method based on smoothed particles hydrodynamics (SPH) method and offering the possibility, among other applications, to describe accurately slamming case features. SPH method is a recent scheme that was first designed for astrophysics problems [1,2]. This method has been then adapted in order to include the presence of a free surface in fluid flow simulations [3], and finally turned out to be an interesting tool for describing these kind of problems. Thanks to its meshless and Lagrangian characteristics, simulations of breaking and reconnection of the interface can be easily handled, that is to say in overcoming the problems of mesh management usually encountered in classical mesh

* Corresponding author.
E-mail address: guillaume.oger@ec-nantes.fr (G. Oger).

0021-9991/$ - see front matter
doi:10.1016/j.jcp.2005.09.004

based methods dedicated to free surface flow computations. Indeed, the capability of this method to treat efficiently some complicated and large free surface deformation problems has now been evidenced [4,5]. Moreover, its meshless and Lagrangian features allow to solve easily problems including any imposed motion of one or several bodies in the flow. Recent works [6] showed the possibility for this method to be enhanced with a specific treatment to deal with freely moving boundaries in coupled interaction with water. This is achieved through a dedicated method presented here, combining SPH with a procedure aiming at extracting the boundary pressure distribution from near-flow instantaneous characteristics. The pressure evaluation method used is described and a comparison between our SPH solution, the analytical solution given by Zhao et al. [7] and experimental results is provided through the test case of a wedge in imposed motion impacting the free surface. A second study aims at extending this method to a fluid rigid-structure coupling that is discussed and validated through two wedge free surface impacts. The first one is a free fall impact of a wedge with a 30° deadrise angle [7] and the vertical linear motion as the only one degree of freedom. For this case, the slamming force time history of the impact obtained using our enhanced SPH method is compared with experimental and analytical results. The second test case studied then consists in the impact of a free-falling asymmetric wedge with a 20° deadrise angle [8] and three degrees of freedom, namely the vertical and horizontal linear motions (this last will not be discussed), and the angular motion in the vertical plane.

2. SPH method for compressible fluid flow

2.1. Basic equations

SPH method is based on a set of interpolating points which are distributed in the medium. By means of an interpolation function (kernel function), these points can be used to discretize partial differential equations without any underlying mesh. For free surface flows, the system of equations we need to solve is the classical Navier–Stokes one. But since we always assume the fluid to be non-viscous in the applications presented here, shear stresses are neglected and this system reduces to Euler equations as follows:

$$\frac{\mathrm{d}\vec{v}}{\mathrm{d}t} = \vec{g} - \frac{\vec{\nabla}P}{\rho}, \tag{1}$$

$$\frac{\mathrm{d}\rho}{\mathrm{d}t} = -\rho\vec{\nabla}\cdot\vec{v}, \tag{2}$$

where $\vec{g}$, ρ, P and $\vec{v}$ stand, respectively, for the body forces, the density, the pressure and the velocity throughout the fluid medium.

One of the main SPH features consists in considering any fluid flow as compressible, resulting in the use of an equation of state. In this paper we used the following equation:

$$P = \kappa\left[\left(\frac{\rho}{\rho_0}\right)^{\gamma} - 1\right], \tag{3}$$

called Tait's equation (3), linking the pressure to the density and allowing the above system of equations to be closed.

The use of this equation of state allows to avoid an expensive resolution of the Poisson equation and incompressible flows are obtained as weakly compressible ones. The constant κ refers to the sound speed in the fluid medium and comes from $c_0^2 = \frac{\mathrm{d}P}{\mathrm{d}\rho}|_{\rho=\rho_0}$, that is $\kappa = \frac{c_0^2\rho_0}{\gamma}$, where c_0 is the nominal value of the chosen sound speed, ρ_0 the nominal density value and γ the polytropic constant.

Note that c_0 is usually arbitrarily chosen and generally differs from the actual sound speed of the considered fluid. Actually, if the field Mach number remains sufficiently low (below 0.1) during the whole simulation, the SPH solution remains in the vicinity of the incompressible solution [3]. Indeed the stability properties of SPH are clearly related to the local sound speeds so that simulating a nearly incompressible fluid, having a high sound speed such as water, would lead to very small time steps, increasing considerably the computational cost.

c_0 is commonly chosen applying

$$c_0 = \frac{V_{\max}}{Ma}, \tag{4}$$

where $V_{\max}$ is the highest fluid velocity and Ma the yield Mach number. In this condition, the density will not differ from more than one percent of the nominal density value ρ_0.

2.2. SPH formulation

2.2.1. Interpolation scheme

The fundamental basis of the SPH framework is the interpolation procedure [2]. In the absence of mesh, one needs to determine the Lagrangian derivative $\frac{\mathrm{d}\rho}{\mathrm{d}t}$ and $\frac{\mathrm{d}\vec{v}}{\mathrm{d}t}$ for each point of the fluid domain in order to proceed to the time integration. The knowledge of $\rho\vec{\nabla}\cdot\vec{v}$ and $\frac{\vec{\nabla}P}{\rho}$ is thus needed at these points. These space derivatives are determined through the use of a kernel function into a finite domain surrounding each point of interest, each of these points being carrying the discrete fluid quantities ρ, P and $\vec{v}$.

Considering a given function f, it is possible to convolute it using its values and a chosen kernel function within a compact kernel support D proportional to the so-called smoothing length, noted h, standing for the meshless equivalent of a space step employed in classical mesh based methods. We thus write

$$f(\vec{r}) \approx \int_D f(\vec{x}) W(\vec{r}-\vec{x}, h)\,\mathrm{d}\vec{x}, \tag{5}$$

where D is a circular or a spheroidal domain in a two- or three-dimensional context respectively. In this study, due to the kernel function we chose, D is defined with a radius equal to $2h$.

The approximation (5) makes sense provided that the kernel function W becomes a delta function in the limit $h \to 0$, making approximation (5) to tend towards a strict equality.

The gradient of any function f can be approximated by applying (5), leading to

$$\vec{\nabla} f(\vec{r}) \approx \int_D \vec{\nabla} f(\vec{x}) W(\vec{r}-\vec{x})\,\mathrm{d}\vec{x}. \tag{6}$$

Finally, thanks to integration by parts of (6), and neglecting the surface term using the compact support property of W, this equation reduces to

$$\vec{\nabla} f(\vec{r}) \approx \int_D f(\vec{x}) \vec{\nabla} W(\vec{r}-\vec{x})\,\mathrm{d}\vec{x}, \tag{7}$$

after integration by parts.

2.2.2. Numerical integration

We need to formulate the previous integrals in a discrete approximation. This is done through the following quadrature formula:

$$\int_D g(\vec{x})\,\mathrm{d}\vec{x} \approx \sum_i g_i \omega_i, \tag{8}$$

where i refers to each interpolating point within the domain D. Note that a weight term ω_i appears in this quadrature formula. This term has the dimension of a volume, and from the volume conservation equation (9) on the one hand and the continuity equation (2) on the other hand, it can be noticed that the product $\rho\omega$ remains constant in time. Thanks to this property, the concept of 'particles' can be introduced, each interpolation being not only a calculation point, but also a 'particle' carrying a constant mass $\rho_i\omega_i$ [9],

$$\frac{\mathrm{d}\omega}{\mathrm{d}t} = \omega \cdot \vec{\nabla}\vec{v}. \tag{9}$$

Eq. (7) is discretized following:

$$\langle \vec{\nabla} f(\vec{r}) \rangle_i = \sum_j f(\vec{r}_j) \vec{\nabla} W(\vec{r}_i - \vec{r}_j, h) \omega_j. \tag{10}$$

Finally, the formulation used in this paper is the following one [2]:

$$\frac{\mathrm{d}\vec{x_i}}{\mathrm{d}t} = \vec{v_i}, \tag{11}$$

$$\frac{\mathrm{d}\vec{v_i}}{\mathrm{d}t} = \vec{g} - \sum_j m_j \left(\frac{P_i}{\rho_i^2} + \frac{P_j}{\rho_j^2}\right) \vec{\nabla} W(\vec{x_i} - \vec{x_j}, h), \tag{12}$$

$$\frac{\mathrm{d}\rho_i}{\mathrm{d}t} = \sum_j m_j (\vec{v_i} - \vec{v_j}) \vec{\nabla} W(\vec{x_i} - \vec{x_j}, h). \tag{13}$$

This scheme does not explicitly need to impose some kinematic free surface conditions thanks to the Lagrangian motion of particles. In the present study, no specific procedure aiming at enforcing the dynamic free surface conditions has been implemented, even if such treatment would be of great interest.

2.2.3. Numerical stability

The SPH scheme naturally suffers from a lack of stability due to its explicit time integration, combined with a space centered like feature [9]. In order to increase the numerical stability properties of this method, an artificial viscosity term is added in the momentum equation following Monaghan [2], that is

$$\Pi_{ij} = \begin{cases} -\alpha \frac{\bar{h}_{ij} \bar{c}_{ij}}{\bar{\rho}_{ij}} \frac{\overrightarrow{v_{ij}} \cdot \overrightarrow{r_{ij}}}{r_{ij}^2 + \epsilon \bar{h}_{ij}^2} & \text{if } \overrightarrow{v_{ij}} \cdot \overrightarrow{r_{ij}} < 0, \\ 0, & \text{else,} \end{cases} \tag{14}$$

where any value $\bar{f}_{ij}$ denotes $\frac{f_i + f_j}{2}$.

The main drawback of this term is that it brings additional dissipation [10] in the global scheme. It is a problem namely for relatively low-dynamics flows where good energy conservation properties are required, whereas it is not so restrictive for violent-dynamics flows provided that the non-dimensional viscosity parameter α is chosen as small as possible.

Another classical instability, the so-called tensile instability, may appear in SPH calculations, but no relevant effect has been found in the results presented in this paper.

Finally, the resulting ordinary differential equation system can be integrated in time by schemes such as Runge–Kutta, Leap–Frog or any Predictor–Corrector, to ensure at least second order convergence in time. Nevertheless, special cares have to be paid at the time steps used [2], which are defined following a Courant condition based on the local smoothing length, the local sound speed and which takes into account the artificial viscosity contribution so that

$$\delta t = K \cdot \min_i \left[\frac{h_i}{c_i \cdot (1 + 0.6\alpha)} \right]. \tag{15}$$

A comparative study with Runge–Kutta methods of different orders proved the advantages of using methods of order greater than two: the loss in CPU time due to the increased number of second member evaluations is more than balanced by the increase in the acceptable value for the constant K to conserve stability, resulting finally in a decreased total CPU time. In the simulations presented here, a third order Runge–Kutta scheme was used, with $K = 0.23$. Despite this value seems to be rather small once compared with values usually mentioned in the literature, many tests confirmed this constant to give some good stability properties on a wide range of applications.

2.2.4. Variable smoothing length

In the context of astrophysics studies, Monaghan introduced the notion of spatially varying resolution [2], in which the smoothing length adapts according to the local number density of particles. Various studies aiming at improving the formulation and confirming the efficiency of this extension of the SPH algorithm has been carried out [11,12].

More than allowing to cope with these specific astrophysics problems, this technique turns out to be an interesting tool for a more general use in fluid mechanics. Indeed, in lots of cases we do not need high

accuracy everywhere in the fluid domain studied (which would lead to an expensive calculation) but only in a given area. It is namely the case for the simulation presented here, where we need accuracy in the impact area only. Thus, the smoothing length h is initially distributed so that its values are small in the desired accurate area and bigger elsewhere, leading to a method quite equivalent to local refinement/stretching commonly used in mesh-based Navier–Stokes solvers. Formally, these features imply some additional terms involving $\vec{\nabla}h$ and $\frac{\mathrm{d}h}{\mathrm{d}t}$ in the previous formulation [11–13] aiming at satisfying conservation requirements.

The $\frac{\mathrm{d}h}{\mathrm{d}t}$ term stands for the Lagrangian derivative of h. In this paper, each particle carries its own smoothing length which does not vary in time, so that this term is always equal to zero. On the contrary, the terms involving $\vec{\nabla}h$ are non-zero since particles of bigger and smaller smoothing lengths meet together during their Lagrangian evolution. But for the sake of simplicity, these terms were not implemented in our SPH formulation. Thus, in order to limit the amount of errors in the present study, the particle setup was chosen so that the smoothing length varies slowly in space on the one hand, and local areas needing high accuracy was preferred to be discretized with a constant smoothing length on the other hand.

Two kinds of interpolation have been introduced in the context of variable smoothing length: the gather and the scatter formulations first discussed by Hernquist and Katz [11].

The gather formulation is defined as

$$f^{\mathrm{g}}(\vec{r}) = \int_D f(\vec{x}) W(\vec{r} - \vec{x}, h(\vec{r}))\,\mathrm{d}\vec{x}, \tag{16}$$

whereas the scatter one corresponds to

$$f^{\mathrm{s}}(\vec{r}) = \int_D f(\vec{x}) W(\vec{r} - \vec{x}, h(\vec{x}))\,\mathrm{d}\vec{x}. \tag{17}$$

We choose to discretize the continuity equation (2) using the gather form, that is

$$\frac{\mathrm{d}\rho_i}{\mathrm{d}t} = \sum_j m_j(\vec{v}_i - \vec{v}_j)\vec{\nabla}W(\vec{r}_i - \vec{r}_j, h_i). \tag{18}$$

Bonet et al. [14] showed that, by derivation of a stored energy functional, it is possible to link the mass conservation equation formulation with the final form to adopt for the momentum equations. In deed, from the choice of the mass conservation discretization, we are led to specific discretized momentum equations.

We extend here the variational framework adopted by Bonet et al. [14] to a coherent variable smoothing length formulation for the disretized continuity and momentum equations, and refer the reader to for a complete understanding of the following study.

We start with

$$D\Pi[\delta\vec{v}] = \sum_{i=1}^{N} \vec{T}_i \cdot \delta\vec{v}_i, \tag{19}$$

applied on a large set of N particles carrying a constant masse m_i, where $D\Pi[\delta\vec{v}]$ denotes the variation of the total stored energy functional Π introduced in [14], and $\vec{T}$ and $\delta\vec{v}$ represent, respectively, the equivalent internal forces due to the state of stress inside the fluid and the virtual velocity field.

Opposite to Bonet et al., we take here

$$\bar{\bar{\sigma}} = -P\bar{\bar{I}}, \tag{20}$$

where $\bar{\bar{\sigma}}$ is the isotropic stress tensor and P the pressure. (Note that a positive pressure indicates compression throughout this paper, as usually observed in fluid mechanics.)

The Newton's second law gives in these conditions

$$m_i \frac{\mathrm{d}\vec{v}_i}{\mathrm{d}t} = \vec{T}_i + \vec{g}. \tag{21}$$

We adopt the following gather formulation for the density equation

$$\rho(\vec{x}) = \sum_{j=1}^{N} m_j W(\vec{x} - \vec{x}_j, h), \tag{22}$$

since h represents here the smoothing length at point $\vec{x}$, and we finally obtain after derivation

$$D\rho_i[\delta\vec{v}] = \sum_{j=1}^{N} m_j \vec{\nabla} W(\vec{x}_i - \vec{x}_j, h_i) \cdot (\delta\vec{v}_i - \delta\vec{v}_j). \tag{23}$$

Recalling

$$D\Pi[\delta\vec{v}] = -\sum_{i=1}^{N} m_i \left(\frac{P_i}{\rho_i^2}\right) D\rho_i[\delta\vec{v}], \tag{24}$$

and since $\vec{\nabla} W(\vec{x}_i - \vec{x}_j, h_j) = -\vec{\nabla} W(\vec{x}_j - \vec{x}_i, h_j)$, we easily obtain

$$\begin{aligned} D\Pi[\delta\vec{v}] &= -\sum_{i=1}^{N}\sum_{j=1}^{N} m_i m_j \left(\frac{P_i}{\rho_i^2}\right) \vec{\nabla} W(\vec{x}_i - \vec{x}_j, h_i) \cdot (\delta\vec{v}_i - \delta\vec{v}_j) \\ &= \sum_{i=1}^{N} \left[\sum_{j=1}^{N} -m_i m_j \left(\left(\frac{P_i}{\rho_i^2}\right) \vec{\nabla} W(\vec{x}_i - \vec{x}_j, h_i) - \left(\frac{P_j}{\rho_j^2}\right) \vec{\nabla} W(\vec{x}_j - \vec{x}_i, h_j) \right) \right] \cdot \delta\vec{v}_i. \end{aligned} \tag{25}$$

Thus, using Eq. (18) one needs to discretize the momentum conservation equation following:

$$\frac{\mathrm{d}\vec{v}_i}{\mathrm{d}t} = \vec{g} - \sum_j m_j \left(\frac{P_i}{\rho_i^2} \cdot \vec{\nabla} W(\vec{x}_i - \vec{x}_j, h_i) - \frac{P_j}{\rho_j^2} \cdot \vec{\nabla} W(\vec{x}_j - \vec{x}_i, h_j) \right), \tag{26}$$

where appears a mixing of gather and scatter derivatives. Similar conclusions can be obtained by alternative analysis based on conservation law studies, as shown by Vila [9]. Note that (18) does not provide symmetrical interactions for $h_i \neq h_j$. On the contrary, Eq. (26) systematically results in a symmetrical interaction even in the case of non-reciprocal neighborhood.

2.2.5. Search algorithm

For each particle, we need to compute interactions with its neighbors. Because of the compact support property of the kernel function, these interactions are non-zero only within an interpolating radius of $2h$. Using this property, and in order to limit the computational cost, a specific neighbor search algorithm had to be implemented. In the search algorithm classically mentioned in SPH related literature [15], particles are stored in an underlying cartesian grid composed of square cells with a size equal to the interpolating radius (Fig. 1). In order to find the neighbors of a given particle of interest i as efficiently as possible, one just needs to

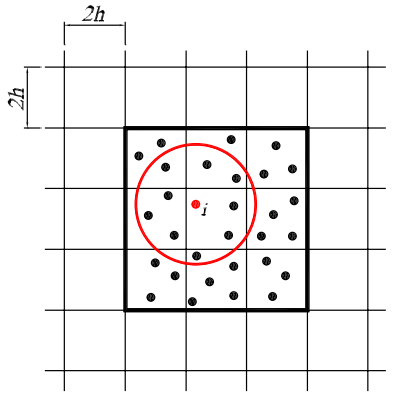

Fig. 1. Underlying grid.

list the particles contained in its cell, as well as in the eight cells around it (cells within the bold square in Fig. 1). Thus, only particles likely to be in the interpolating area are tested, and any chance of missing an interaction is avoided. Because of particle motions, the grid needs to be periodically updated in order to avoid any missing interaction. It should be emphasized that this underlying grid is exclusively used for the neighbor search procedure.

This search procedure is responsible for a non-negligible CPU time. On the other hand, it can be noticed that the typical time steps used in SPH method remain rather small, and consequently the particle displacements between two successive neighbor search procedures are very small. This particularity implies that the neighborhood changes are quite occasional, giving a possibility of additional improvements on the neighborhood creation. Indeed, rather than to renew the interaction list at each Runge–Kutta step, it is possible to make an interaction list that could be valid for several time steps, leading to a large decrease of necessary CPU time. To operate in this way, the interaction list is composed using the search algorithm previously described, but this time, the neighbor particles must be contained within a radius bigger than the interpolating one. This bigger radius aims at storing in advance the potential neighbors, in order to allow the search procedure not to be done systematically, and still without any risk of missing interactions. Let us call $R = 2h + \varepsilon$ this radius, and $V_{\max}$ the maximum velocity reached throughout the fluid flow simulation involved. The value ε is chosen so that, in a cartesian particle distribution, the neighbor number does not differ from the one obtained in a radius equal to $2h$. Taking the most pessimist case, for example a given particle k in Fig. 2, having a velocity $\vec{V}_k = -V_{\max} \cdot \vec{x}$ and placed right out of R, and calling Δt the time between two consecutive search procedures, the safety criterion to ensure that the k/i interaction will be taken into account when particle k enters the $2h$ interaction radius is given by

$$\Delta t < \frac{V_{\max}}{\varepsilon}. \tag{27}$$

This method, known in the literature as "Verlet table" [16,17], offers here a large decrease of CPU time, especially for calculations involving a strong dynamics, where time steps remain small. In the context of variable smoothing length, since the cell sizes may differ from the interpolation radius, the number of cells to be explored is greater than nine (depending on the smoothing length of the particle of interest), leading to a decrease of the neighbor search algorithm efficiency.

2.2.6. Boundary conditions

The treatment of boundary conditions remains one of the main subtleties of the SPH method. Various approaches are possible for implementing boundaries, for instance the so-called repellent particles [3].

We finally adopted the ghost particle method as free slip boundary conditions. In this method, water particles within a distance $2h$ from the wall are mirrored across the boundary following its local normal. These image particles are called "ghost particles", and their characteristics (velocity, pressure and smoothing length) are determined using the fluid particle ones, following:

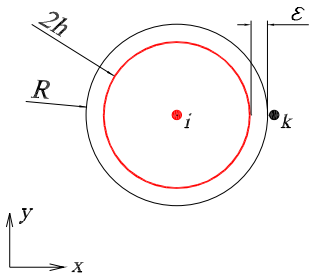

Fig. 2. Enlarged radius.

$$P_{G_i} = P_i, \tag{28}$$

$$v_{n_{G_i}} = (2\vec{V}_{\mathrm{M}} - \vec{v}_i) \cdot \vec{n}, \tag{29}$$

$$v_{t_{G_i}} = \vec{v}_i \cdot \vec{t}, \tag{30}$$

$$h_{G_i} = h_i, \tag{31}$$

where the subscripted term G_i refers to the ghost particle mirroring the fluid particle i. $\vec{V}_{\mathrm{M}}$ stands for the local velocity of the boundary at M, this point being the projection of particle i following the local normal $\vec{n}$. v_{n} and v_{t} correspond to the normal and tangential velocities, respectively. Eqs. (30) and (29) ensure a free slip and a non-penetration boundary conditions, respectively.

The use of ghost particles results in a robust treatment of boundary conditions, provided that some subtleties concerning the mirroring of particles for boundaries owning singular geometries such as sharp angles are implemented. Indeed, special care has to be paid in such corners, where a systematic mirroring of water particles would bring some excess of ghost mass, as discussed in [18].

3. Local pressure evaluation procedure

Lots of general fluid problems require the knowledge of local pressure on solid boundaries. Besides, this specific point (for which obtaining correct results is not so obvious) is unusually approached in the SPH related literature. We aim here at presenting a method allowing a possible approach of this topic.

As previously outlined, the standard SPH method suffers from a lack of stability that is alleviated using an artificial viscosity term π_{ij}. Actually, this term helps in obtaining an increase of regularity of the pressure field everywhere in the fluid domain. Note that even when we use this additional term, some pressure irregularities subsist, making the pressure estimation to be a subtle task, mainly in near boundary areas. Some improvements on the pressure distribution are possible, as discussed by Colagrossi et al. [18], by periodic density re-initialization using a second order accurate interpolation through a moving least square kernel. This method has not been employed here, this in order to study the standard SPH scheme behavior in a first attempt. Nevertheless this kind of enhancement is always possible and should give some very interesting results for the application described here.

We tried various techniques for extracting correct local pressures, namely by using the kernel function convolution at a desired boundary point $\vec{r}$, that is,

$$\langle P(\vec{r}) \rangle = \sum_j P(\vec{r}_j) W(\vec{r}_i - \vec{r}_j, h) \omega_j. \tag{32}$$

We expected this SPH-coherent interpolation to give a reasonable estimation of the pressure field, but only few particles contribute in this procedure, resulting in high stability requirements in our computation. Our tests leaded finally to some crude results. Here again, a periodic density or pressure re-initialization may be a possible solution to this problem, but this has not been tried here.

Finally, we propose a new technique that gave the most interesting results for the local pressure evaluation. We aim at estimating the local pressure at a given point M (Fig. 3). This value is extracted from SPH particles (excepted ghost particles) in the near boundary area around M.

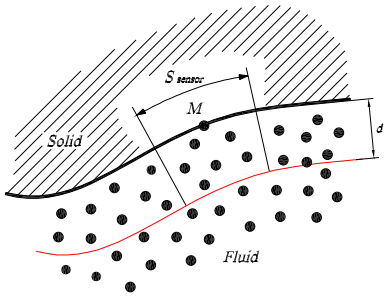

Fig. 3. Sampling area.

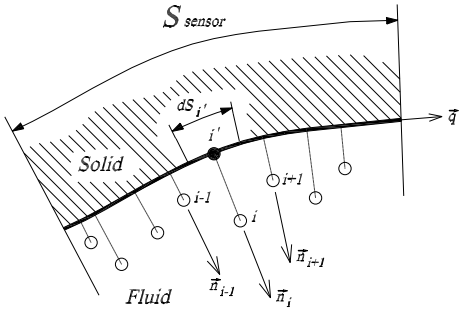

Fig. 4. Particle sampling.

This area is an image of a pressure distribution that would be seen by a pressure sensor during a physical experiment. This local pressure is taken as

$$P_{\mathrm{M}} = \frac{\int_{S_{\mathrm{sensor}}} P \,\mathrm{d}S}{\int_{S_{\mathrm{sensor}}} \mathrm{d}S}. \tag{33}$$

Formally, the approximation P_{M} tends to the exact pressure at point M as the sensor surface narrows.

In order to approximate formula (33), particles are first sampled in the near boundary area (Fig. 4), within a distance d from the boundary that is proportional to the smoothing length h, and within the width S_{sensor} of the sensor. Each sampled particle i is then projected i' following a direction normal to the local boundary surface. These particles are then sorted in tangential position order, evolving along the curvilinear abscissa $\vec{q}$.

Surface elements $\mathrm{d}S$ are then determined using

$$\mathrm{d}S_{i'} = \frac{q_{i'+1} - q_{i'-1}}{2}, \tag{34}$$

where $q_{k'}$ is the curvilinear abscissa of k', particle k being the kth particle sampled in the curvilinear progression.

Thus, some numerous particles contribute in the estimation of the boundary pressure at M, giving a correct approach of the mean pressure at this point, by using a high number of small surface elements $\mathrm{d}S$. Then, formula (33) is approximated using a trapeze like quadrature formula that is

$$P_{\mathrm{M}} \simeq \frac{\sum_{i'} P_{i'} \,\mathrm{d}S_{i'}}{\sum_{i'} \mathrm{d}S_{i'}}, \tag{35}$$

where i' denotes the projected point of particle i.

Since the pressure field is not taken exactly on the boundary but near it, some errors occur, in particular on the hydrostatic component of the pressure (due to the vertical distance between the particle i and its projection i'). That is why $P_{i'}$ is taken as

$$P_{i'} = P_i - \rho_i g (y_{i'} - y_i), \tag{36}$$

where y denotes positions along the gravity direction. Formally, this projection distance would also involve a $\frac{\mathrm{d}\vec{V}}{\mathrm{d}t} \cdot \vec{n}$ correcting term ($\vec{n}$ being the local normal to the boundary), but this correcting term were not implemented is the present study.

4. Test case of a symmetric wedge impact in imposed motion

In order to study the efficiency of this local pressure evaluation method, we apply it to the validation test case of a symmetric wedge impacting the free surface. This experiment has been carried out by Zhao et al. [7], and the motion experimentally recorded is imposed as an input of the simulation presented here.

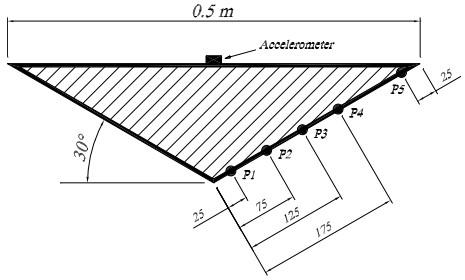

Fig. 5. Test section description.

4.1. Drop test description

At $t = 0$ s, this wedge is dropped against calm water, entering the free surface with a 6.15 m/s initial vertical velocity. This impact generates a large free surface deformation, accompanied by the apparition of two jets running out along the wedge boundaries, and imposing a strong vertical deceleration of the solid. Despite the existence of three-dimensional effects in this experiment, the flow is regarded here as two-dimensional. The test section used in the experiments is described in Fig. 5.

The length of this wedge is 1.0 m. It is fitted with piezoresistive pressure cells of diameter 4 mm (P1–P5 in Fig. 5). The vertical force was measured using two force transducers connecting the test section to the drop rig. Vertical acceleration was measured using an accelerometer placed at the top of the test section, and vertical velocity was obtained using an optical sensor. Finally, the vertical velocity time history results from a combination of values given by both the accelerometer and the optical sensor. The vertical motion is the only degree of freedom allowed to the wedge in this experiment. More details can be found in [7].

4.2. Numerical simulation

In the SPH simulation, the numerical setup has been adapted. Indeed, the impact on water generates a sound wave that reaches the tank boundaries. The reflection of this sound wave then goes back to the wedge and may interact with it. Thus, the tank size has been chosen to ensure no interaction between the wedge and this reflected sound wave, at least during the period of interest of this impact. In order to ensure a near incompressible simulation with $Ma < 0.1$, the nominal sound speed chosen for the water is 80 m/s. In this circumstance, taking into account the previous note, the distance between the impact area and the tank boundary has been chosen to be 3.6 m. The equation of state (3) used for water is computed with the polytropic constant $\gamma = 7$. This simulation has been made without the presence of air, and as a consequence the outside pressure P_0 is taken to be 0. The nominal density used for water is $\rho_0 = 1000$ kg/m^3. The numerical initial conditions for the SPH wedge were defined using the exact velocity and position of the experimental test section at the impact instant.

Throughout this study, and whatever the chosen smoothing length value, the typical distance (noted Δx) between two particles is determined so that the interpolation circle contains about 20 particles (in a two-dimensional context), that is,

$$\frac{h}{\Delta x} = 1.23. \tag{37}$$

Using this tank size, and taking into account the accuracy needed for this test case, a constant smoothing length would lead to a very high number of particles, inducing a high computational cost. Thus, as previously indicated, we use a variable smoothing length and concentrate all the accuracy in the impact area.

In order to limit the total amount of errors induced by the asymmetrical character of the variable smoothing length formulation, the smoothing length is defined as constant everywhere in the desired accurate area. This area is shown (hatched zone) in Fig. 6.

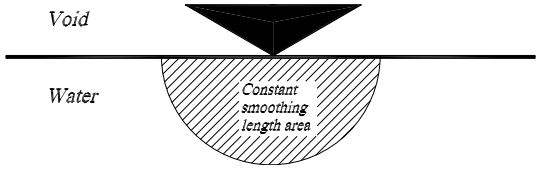

Fig. 6. Numerical setup.

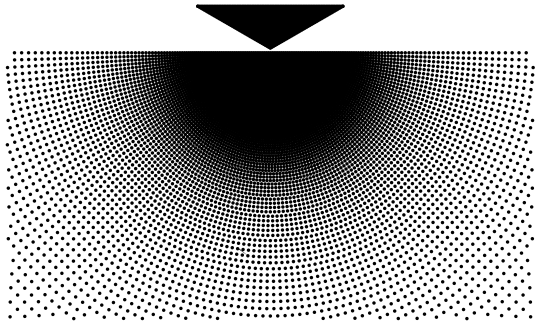

Fig. 7. Detail of the initial particle setup.

Out of this zone, particles are distributed so that h (as well as Δx) increases slowly from the limit of the constant smoothing length area up to the tank border; the ith particle, counted radially from the limit of the constant-h area, has its smoothing length defined as

$$h_i = 1.03^i h_0, \tag{38}$$

where h_0 is the smoothing length in the hatched zone.

Some tests proved the constant 1.03 to be the highest value admissible to prevent any undesirable numerical effects. Bigger values would lead to inner reflected sound waves due to the absence of correcting terms, mainly the $\vec{\nabla}h$ term. The initial particle set up corresponds here to a radial distribution (see Fig. 7), this for the sake of simplicity in implementing the initial particle positions.

The use of the variable smoothing length method results in a dramatic decrease of the global particle number necessary for this simulation. For instance, the tank previously presented would need about 21,400,000 particles for $h = 0.0012$ m, which is reduced to only 200,000 necessary particles for $h_0 = 0.0012$ m in the variable smoothing length context.

4.3. Local SPH pressure validation in the case of experimental imposed motion

Willing to validate our scheme, we compared the results given by the local SPH pressure evaluation method previously exposed with experimental and analytical results given by Zhao et al.

To this purpose, in the SPH simulation, the motion of the wedge is entirely governed by the experimental motion of the test section. Indeed, the simulation was achieved taking for wedge velocity the velocity experimentally measured in [7], and reported in Fig. 8.

One of the main difficulties in this method relies in the choice of the value to give to the particle sampling distance d (see Fig. 3). In order for the pressure evaluation procedure to converge, this distance needs to depend on the smoothing length, so that it tends towards zero as the smoothing length h decreases.

We tried various values for the distance d, using $h_0 = 0.0012$ m, and systematically compared our SPH local pressure to Zhao's analytical and experimental pressure results, at three given instants, $t = 0$ s being the instant when the wedge touches the free surface. The results are presented in Fig. 9(a)–(c). From left to right, instants shown are $t = 0.00435$ s, $t = 0.0158$ s and $t = 0.0202$ s, respectively.

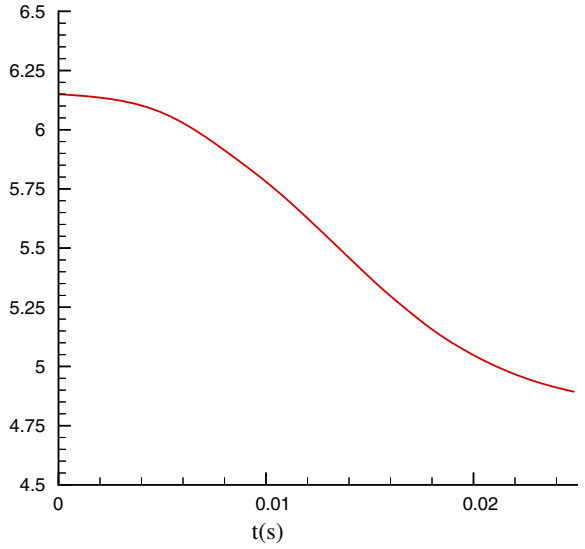

In Fig. 9(a)–(c), P denotes the local pressure, P_0 the outside pressure (which is 0 in the SPH simulation), $V(t)$ the wedge vertical velocity given in Fig. 8, z the vertical coordinate on the wedge surface, z_k the vertical coordinate of the keel and z_D the draft of the body. Note that this notation is the same as the one used by Zhao et al. Dots correspond to experimental pressure results, the dash lines to Zhao's analytical results, and the plain lines to present results. The value S_{sensor} is taken as equal to the pressure cell diameter used in the experiment, that is 4 mm.

These results show that the value taken for d affects the smoothing of the local pressure evolution along the wedge boundary. The higher d is, the smoother the local pressure evolution is, as it would have been intuitively predicted. This smoothing tends globally to slightly lower the pressure numerical estimation. Globally, this test shows that the choice of the parameter d (within reasonable limits) has a weak influence on the results, which validates our procedure to evaluate local pressures on the boundary. Indeed, the choice of d affects the pressure results mainly at the beginning of the impact (left plots in Fig. 9(a)–(c)) and not after. The possible value to adopt for d seems to be included between $5h_0$ and $10h_0$ since some instabilities (high-frequency oscillations) are observed on curves corresponding to $d = 2h_0$.

When compared to Zhao's analytical and experimental results, our local pressure is underestimated for the instant $t = 0.00435$ s, and this whatever the value taken for d. For this instant, the SPH local pressure evolution is not as monotone as Zhao's one, indicating a lack of stability in the SPH near boundary pressure distribution. We suppose this to be due to some compressible effects generated by the sudden change of fluid flow characteristics at the very beginning of the impact. Indeed, this defect disappear for $t = 0.0158$ s, where our results seem to be in quite good agreement with Zhao's analytical ones, except for the maximum load, which is weaker. On the contrary, for $t = 0.0202$ s, our results are clearly overestimated compared with experiments as well as analytical solution. For $t = 0.0158$ s and $t = 0.0202$ s, experimental results P1–P5 are clearly lower than analytical as well as numerical results. This fact is supposed to be due to three-dimensional effects, as mentioned by Zhao et al., explaining these big differences. Globally, this SPH local pressure evaluation method seems to give, in a first attempt, some acceptable results.

5. Extension to a fluid–solid coupling procedure

Thanks to the tests previously presented, it has been proved that it is possible, in a SPH-based computation, to capture the local pressure at any desired point of a boundary with a satisfactory accuracy. As a second step of validation, an interesting way was to integrate these estimated pressures, giving an opportunity of analysis

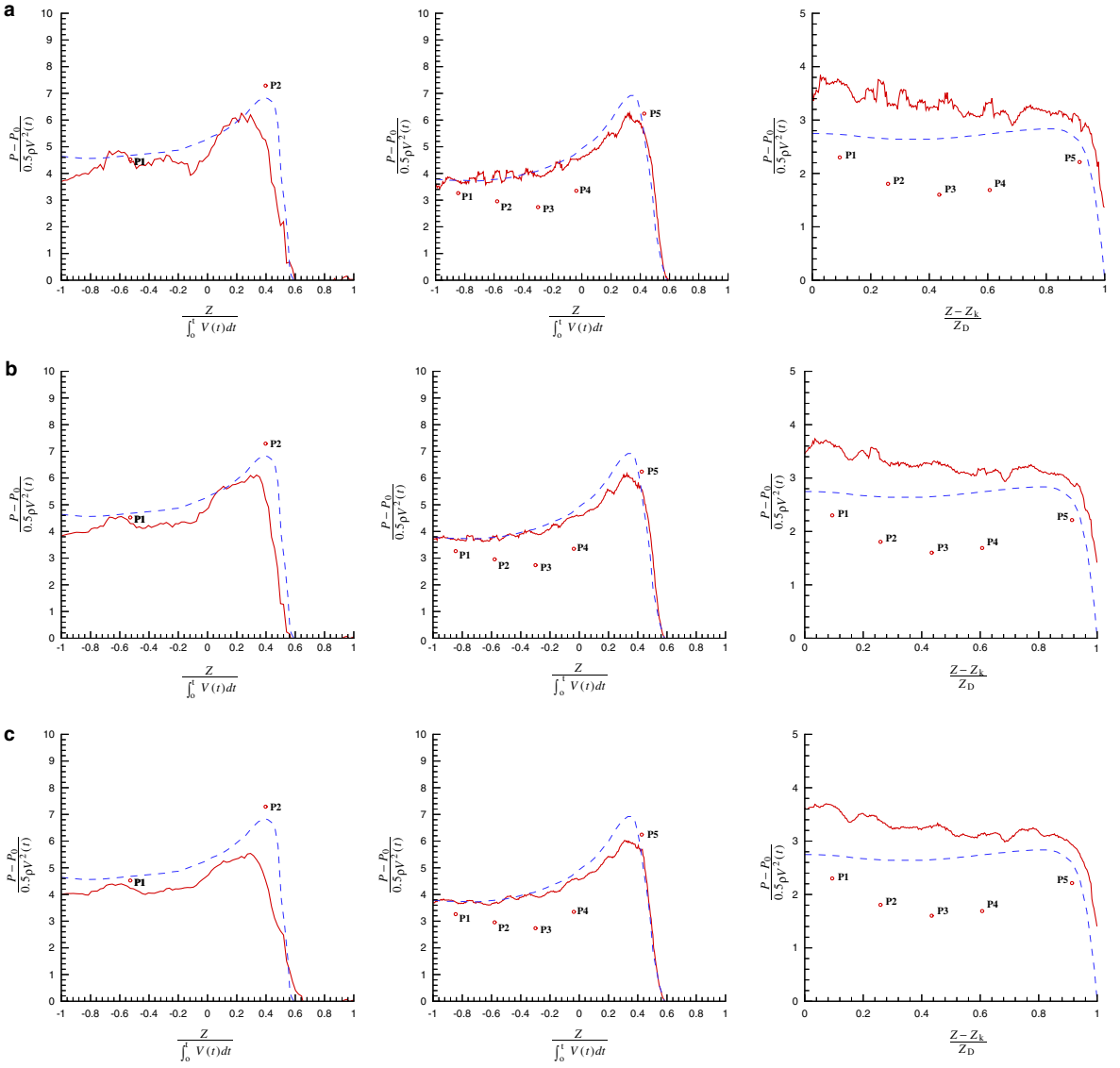

Fig. 9. Comparisons of pressure results. Local pressure results for: (a) $d = 2h_0$; (b) $d = 5h_0$; (c) $d = 10h_0$.

and discussion of this pressure evaluation scheme through achieving the coupling between the fluid dynamics and the rigid body motion, body partially or completely free to move in the flow.

A usual way for simulating this kind of problem using a SPH-based method is to consider the solid as a deformable one, that is to say to treat it as a specific medium in which the stress tensor obeys to the behavior of structures [19,20], this element acting exactly as a given phase in a multi-phase SPH computation [21,22]. But the state equation governing this phase imitates the elastic component of the chosen material. Knowing that the sound speed in metallic materials (for example) operates in the range 4000–5500 m/s, the Courant condition (15) imposes very small time steps, implying a high computational cost. Thus, the scheme presently proposed offers an interesting alternative, where the considered solid is treated as non-deformable, leading to lower CPU time requirements.

We apply here the extension of the local pressure evaluation procedure to fluid–solid coupling test cases, for which some comparisons with experimental results on slamming problems are provided. The main advantage of SPH over other methods for free rigid body–fluid interaction problems resides in the simplicity to treat the

solid motion even in the case of very large movements (entire revolutions for examples), thanks to its meshless property. As well, the introduction of a generic number of solid bodies in a water tank would not induce any additional complications.

We thus need to evaluate, for the general case of a completely free solid in interaction with water, the following integral:

$$\vec{F}_{\text{fluid}\to\text{solid}} = \int_{\delta\Sigma} -P\cdot\vec{n}\cdot \mathrm{d}S, \tag{39}$$

$$M(G)_{\text{fluid}\to\text{solid}} = \int_{\delta\Sigma} -P\cdot\overrightarrow{GI}\wedge\vec{n}\cdot \mathrm{d}S, \tag{40}$$

where $\delta\Sigma$ being the boundaries of the solid Σ, $\vec{n}$ the local normal at the integration point I, G the center of masse of Σ, P and $\mathrm{d}S$, respectively, the pressure and the surface element taken at I.

We then extend the local pressure evaluation procedure to a whole boundary with an undefined shape writing:

$$\vec{F}_{\text{fluid}\to\text{solid}} \simeq \sum_{i'} -P_{i'}\cdot\vec{n}_{i'}\cdot \mathrm{d}S_{i'}, \tag{41}$$

$$M(G)_{\text{fluid}\to\text{solid}} \simeq \sum_{i'} \vec{Gi}'\wedge -P_{i'}\cdot\vec{n}_{i'}\cdot \mathrm{d}S_{i'}, \tag{42}$$

where i' denotes the projected point of particle i. The pressure $P_{i'}$ takes into account the hydrostatic correction previously mentioned.

From the fluid forces acting on the free-solid boundary, we obtain both its linear and angular accelerations writing:

$$\frac{\mathrm{d}\vec{V}}{\mathrm{d}t} = \frac{\vec{F}_{\text{fluid}\to\text{solid}}}{M}, \tag{43}$$

$$\frac{\mathrm{d}^2\theta}{\mathrm{d}t^2} = \frac{M(G)_{\text{fluid}\to\text{solid}}}{I_G}, \tag{44}$$

M and I_G being, respectively, the mass and the inertia taken in G of the solid, and θ its instantaneous angular position. Velocity and position of the considered body are then updated together with flow features using the third order Runge–Kutta scheme used for SPH particles. The main advantage of this method is based on the fact that it does not require a very high resolution (that is to say a very small smoothing length), to allow the capture of solid/fluid coupling effects, due to the high number of sampled particles involved in the treatment. On the other hand, the computational cost needed remains pretty cheap.

6. Test case of a free-falling wedge impact with one degree of freedom

In order to test the efficiency of this procedure, we apply it to the case of water entry previously used but, this time, the dynamics of the wedge is entirely governed by the numerically predicted accelerations extracted from the pressure distribution along the boundary, instead of the previous imposed motion based on the experimental velocity. Since no angular and horizontal motion are allowed in the experiments, only the vertical acceleration is treated.

The results of vertical forces due to water on the wedge are compared to experimental and analytical data given by Zhao et al. in Fig. 10. For this test, a sampling distance $d = 5h_0$ was retained. The SPH slamming force time history is overestimated for $t > 0.01$ s, behavior that is also observed in the analytical solution. This overestimation seems to be due to three-dimensional effects that are not taken into account here and which influence in a significant manner the experimental vertical force (a similar behavior is discussed for instance in [23]). Nevertheless, this result shows an acceptable numerical force estimation when compared with analytical and experimental curves.

Fig. 11(a)–(c) shows the pressure distribution (left plots) along the wedge boundary for the three instants previously mentioned. When compared with pressure results for imposed motion using the experimental veloc-

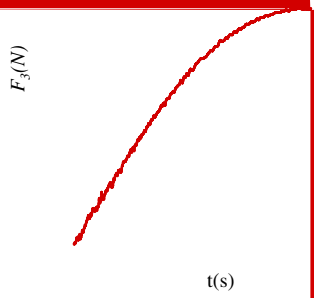

Experiment
Zhao et al. solution
SPH

ity, these results of free-falling wedge give some lower p
tal data. This can be explained by the fact that the nu
one (Fig. 10), leading by time integration to a lower n
As a consequence, the pressure distribution along the w
with experiments than the imposed motion pressure
Fig. 9(a)–(c) were partially due to the imposition of mo
sure distribution has been extracted in a more coheren
effects on the wedge dynamics has been restored.

The smoothing length value used to achieve this co
choice has been made namely in order to allow the jets
cient accuracy. Obviously, the accuracy of the prec
discretization.

Right plots of Fig. 11(a)–(c) provide an illustration
three studied instants. For each of these plots, the pres
field distribution in space around the wedge, and in pa
peaks in the left plots. These pictures offer a visual ex
Fig. 11(a), a pressure non-homogeneity clearly appear
pressure curve at the corresponding instant. Fig. 11(b)
pressure cell P5. Finally, the high-frequency oscillatio
to its corresponding visualization on the right plot.

7. Test case of a completely free-falling wedge impact

7.1. Experimental device

We extend here the previous study to the case of a f
having all its degrees of freedom. The experimental test
wedge are given in Fig. 12 and the wedge initial position
can be found in [8].

At $t = 0$ s, this free-falling wedge is dropped from 0.6
heel angle and no initial velocity. This test section was i
erometers dedicated to the measurement of acceleratio
rated transversely in order to measure the roll dynam
in the air, the wedge enters the free surface. In this case
of two non-symmetrical free surface jets, and this time,
tion of its vertical deceleration. This experiment has be

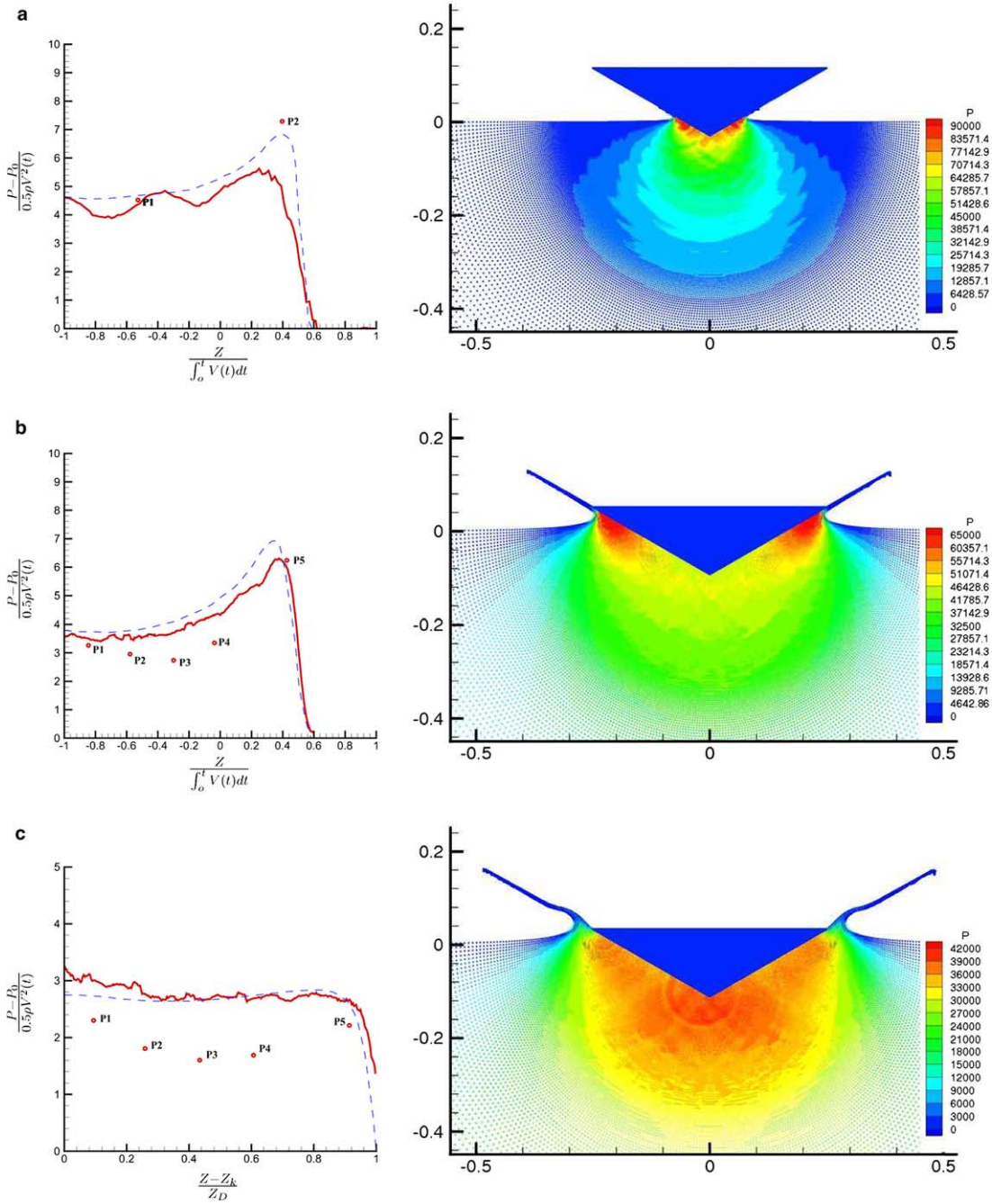

Fig. 11. Non-imposed motion results. Results for non-imposed motion at: (a) $t = 0.00435$ s; (b) $t = 0.0158$ s; (c) $t = 0.0202$ s.

could be regarded as two-dimensional, providing an opportunity of making comparisons between numerical and experimental data in some better conditions than in the previous impact study.

7.2. Numerical simulation

In this test case, the whole dynamics of the wedge is governed by both the interactions with water and the gravity influences. The main difficulty encountered here is based on the coupling appearing between linear and

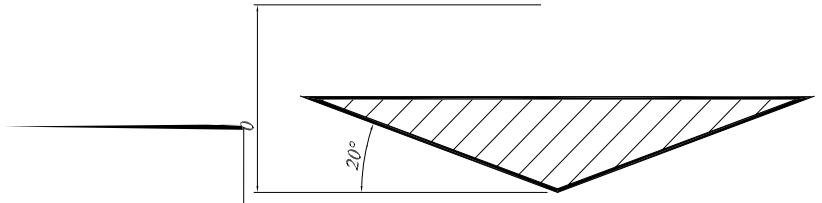

angular accelerations, where any error committed on the angular acceleration, as an example, may have non-negligible effects on linear accelerations, finally leading to possibly large divergences with respect to the experimental results. This simulation has been made with the same tank and particle distribution features as those used in the previous impact case, and with the same fluid properties. Fig. 14 shows the comparison of vertical and angular acceleration time histories (left and right plot respectively) between SPH and experimental results. In order to limit the CPU time, the free fall of this solid is not computed since air is not taken into account: the wedge is placed right above the free surface at the beginning of this simulation, and the numerical initial kinematic conditions for the SPH wedge correspond as much as possible to those of the experimental impact. Note

that because of the errors we made in estimating these initial conditions in our computation, and in order to make the comparison possible, the curves have been matched in time by advancing our SPH results of about 10^{-3} s.

Here, the wedge is flatter than in the previous impact case. As a result, some non-negligible air effects seem to occur at the very beginning of the experimental impact. Indeed, we suppose the progressive evolution of the experimental vertical acceleration from $t_0 = 0.350$ s to $t_1 = 0.355$ s to be due to air cushion effects that can not be captured by our SPH model, presently monophasic. This results in a stiffer vertical acceleration slope than in the experiment from t_1 to $t_2 = 0.360$ s, that can be seen as an occurrence of greater water impact energy. Then, the amplitude of maximum loads reached at $t_3 = 0.365$ s is in good agreement with the experiment. These results have been obtained using a particle sampling distance d taken as $5h_0$, with $h_0 = 0.00095$ m for the smoothing length in the impact area. For such a small value of d, some irregularities appear in the vertical acceleration as well as in the angular acceleration time history, namely at maximum loads instants. Globally, from t_3 to $t_4 = 0.450$ s, the estimated acceleration matches very well the experiment. Two spurious peaks occur in the vertical acceleration, at $t_{sp1} = 0.405$ s and $t_{sp2} = 0.445$ s, respectively. The latter is clearly due to a come

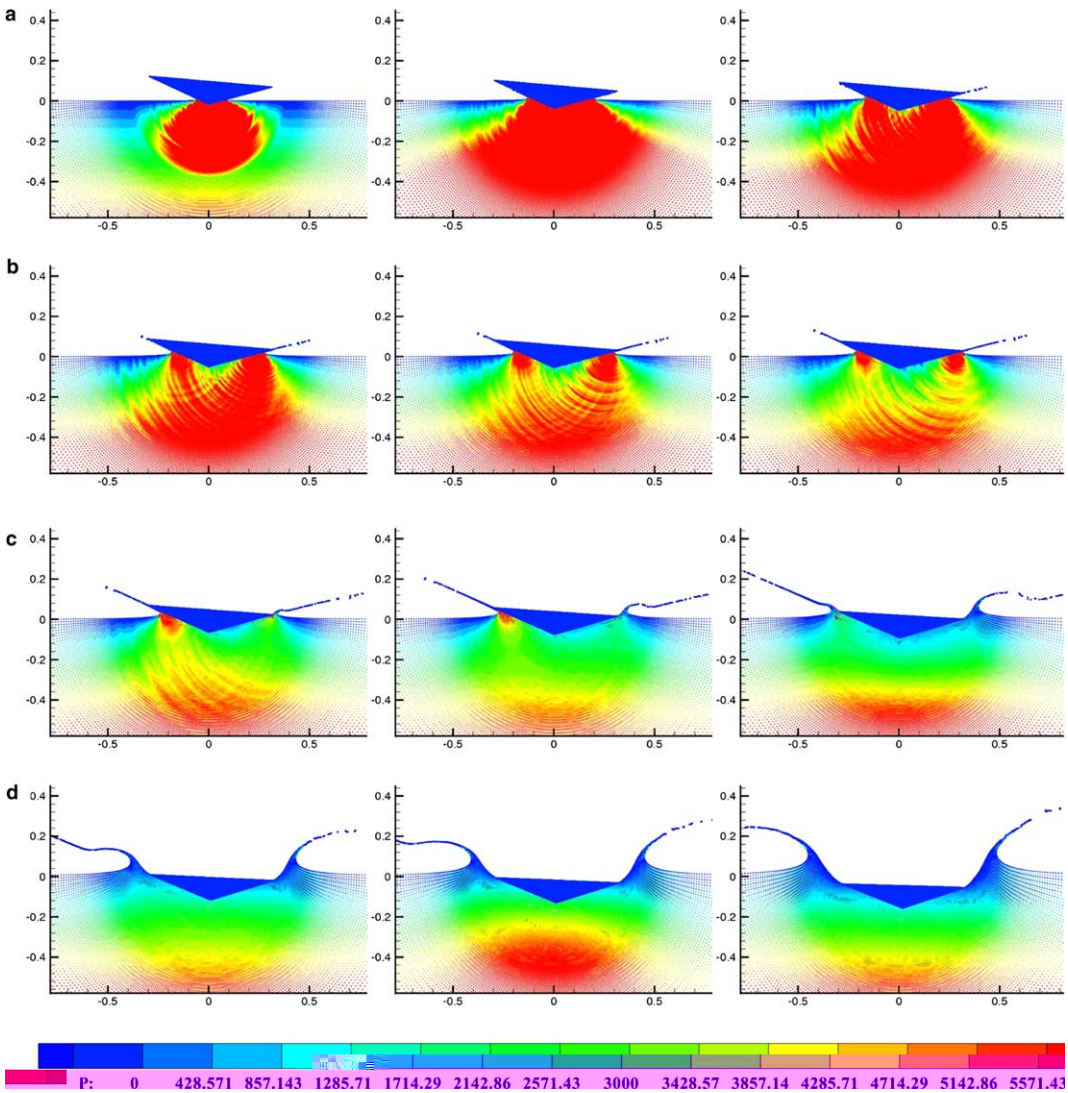

Fig. 15. Asymmetric free surface impact time evolution: (a) $t = 0.2557$ s, $t = 0.25645$ s, $t = 0.25695$ s; (b) $t = 0.2572$ s, $t = 0.25745$ s, $t = 0.2557$ s; (c) $t = 0.2582$ s, $t = 0.25895$ s, $t = 0.4045$ s; (d) $t = 0.4295$ s, $t = 0.4445$ s, $t = 0.477$ s.

back of the reflected impact pressure wave. Indeed, this wave goes back and forth within the water tank, that is a distance 2×3.6 m, covered within $t_{sp2} - t_1$, which corresponds to a mean velocity of 80 m/s, this value being coherent with the nominal sound speed we used for water (we dimensioned the tank size so that this reflected wave reaches the wedge only at the end of the simulation). Concerning the first spurious peak, it can be explained by inner wave reflections due to the sudden smoothing length change occurring at the limit between constant and variable smoothing length areas. This limit seems to behave like a medium that would transmit a big part of the pressure wave but would also reflect it partially. This peak is followed by periodical variations showing the response of the wedge to this abnormal force. Concerning the angular acceleration time evolution, some oscillations can be noticed on the experimental data. These oscillations are produced by structure vibrations which cannot be captured in the context of rigid body simulations [8]. In the SPH computation, oscillations can be explained by temporal fluctuations of values used to obtain efforts on the wedge which may be due to the explicit nature of the third order Runge–Kutta ODE integrator used in this simulation, but further work is still needed to determine the exact origin of this phenomenon. These experimental vibrations make difficult the comparison with the SPH angular acceleration. However, the latter globally matches with the mean experimental signal.

Fig. 15 shows the evolution in time of free surface deformations during the impact, and the pressure scale has again been chosen so that it is possible to observe the near boundary pressure field behavior. It provides the successive shapes of the two non-symmetrical jets generated. One can notice the presence of fragmentation at the tip of these jets. Even if the notion of continuity is violated here, inducing some fundamental errors, the kernel interpolation features of SPH allow the calculation to be achieved without any calculation stop. Note that this fragmentation is an actual physical phenomenon, appearing unavoidably in fluid problems involving a thin fluid volume submitted to a large acceleration as it is the case for the free surface jets occurring here. Note also that no surface tension effects have been implemented in this simulation, but would help in describing accurately the flow in this area.

8. Conclusion

In this paper, a new method designed to extract near solid boundary local pressure in SPH simulations has been presented. This method based on SPH particle sampling has been detailed in the general case of any non-deformable boundary shape. The determination of the sampling distance from the local boundary was needed. In order to determine the optimum sampling distance to retain, and to evaluate the efficiency of this method, its results have been compared with experimental and analytical ones, through the validation test case of a wedge in imposed motion impacting the free surface studied by Zhao et al. The results turned out to show a sensibility on the sampling distance small enough to ensure sufficient accuracy properties, and the sampling distance was finally chosen to be limited to $d = 10h_0$. The SPH predicted local near boundary pressure showed some satisfactory agreements with analytical and experimental ones. This sampling procedure has then been extended to a force evaluation method by pressure integration along the boundary, this in order to treat the complex case of free solids in interaction with free surface fluid flows. This enhanced SPH scheme has been extended to the test of the impact of a free-falling wedge whose vertical linear motion was the only degree of freedom, showing a fair agreement when compared to analytical and experimental results, despite some differences which can be safely attributed to three-dimensional effects in the experiment. Finally, a second test has been carried out, involving the free surface impact of a free-falling wedge having all its degrees of freedom. Again, comparisons between numerical and experimental results have been achieved and discussed. The predicted vertical and angular accelerations were in very good agreement with experimental ones, proving the ability for this scheme to treat accurately some complicated free solid/fluid interactions with a limited computational cost. For this latter case, the main differences observed between numerical and experimental results seem to appear at the very beginning of the impact, finding their origins in air cushion effects that are not implemented in the SPH simulation. Thus, further work is needed concerning the inclusion of air in the SPH solver and the validation of this method on this test case and others. The main advantages of this global scheme combines the high practicability of SPH in terms of implementation (thanks to its meshless property) and the new possibility for this scheme to handle pressure forces acting on non-deformable solid boundaries. The validation of this scheme has been achieved here on free surface impacts, but this method may result in a

very useful tool for a wider range of ocean and coastal engineering applications. It offers a higher simplicity for solving complex hydrodynamic topics such as floating bodies coupled with free surface dynamic responses, sinking vessels in waves, rogue waves impacting structures as a non-exhaustive application enumeration.

References

[1] J.J. Monaghan, R.A. Gingold, Shock simulation by the particle method SPH, J. Comput. Phys. 52 (1983) 374–389.
[2] J.J. Monaghan, Smoothed particle hydrodynamics, Annu. Rev. Astron. Astrophys. 30 (1992) 543–574.
[3] J.J. Monaghan, Simulating free surface flows with SPH, J. Comput. Phys. 110 (1994) 399–406.
[4] A. Colagrossi, M. Landrini, M.P. Tulin, A Lagrangian meshless method for free-surface flows, in: Fourth Numerical Towing Tank Symposium.
[5] Y. Andrillon, M. Doring, P. Ferrant, B. Alessandrini, Comparison between SPH and VOF free surface flow simulation, in: Proceedings of the Fifth Numerical Towing Tank Symposium, 2002.
[6] G. Oger, M. Doring, A. Leroyer, P. Ferrant, B. Alessandrini, SPH and finite volume simulations of a wedge water entry, in: Proceedings of ISOPE'04, 2004.
[7] R. Zhao, O. Faltinsen, J. Aarsnes, Water entry of arbitrary two-dimensional sections with and without flow separation, in: 21st Symposium on Naval Hydrodynamics, 1997.
[8] L. Xu, A.W. Troesch, R. Petterson, Asymmetric hydrodynamic impact and dynamic response of vessels, in: Proceedings of 17th International Conference on Offshore Mechanics and Arctic Engineering, 1998, pp. 98–320.
[9] J.P. Vila, On particle weighted methods and SPH, Math. Model Meth. Appl. Sci. 9 (1999) 161–210.
[10] J.P. Morris, J.J. Monaghan, A switch to reduce SPH viscosity, J. Comput. Phys. 136 (1997) 41–50.
[11] L. Hernquist, N. Katz, Treesph: a unification of SPH with the hierarchical tree method, Astrophys. J. Suppl. Ser. 70 (1989) 419–446.
[12] R. Nelson, J. Papaloizou, Variable smoothing lengths and energy conservation in smoothed particle hydrodynamics, Mon. Not. Roy. Astron. Soc. 270 (1994) 1–20.
[13] J.M. Alimi, A. Serna, C. Pastor, G. Bernabeu, Smooth particle hydrodynamics: importance of correction terms in adaptative resolution algorithms, J. Comput. Phys. 192 (2003) 157–174.
[14] J. Bonet, T.S.L. Lok, Variational and momentum preservation aspects of smooth particle hydrodynamics formulations, Comput. Meth. Appl. Eng. 180 (1999) 97–115.
[15] R.W. Hockney, J.W. Eastwood, Computer Simulation Using Particles, Institute of Physics Publishing, 1988.
[16] L. Verlet, Computer 'experiments' on classical fluids. I. Thermodynamical properties of Lennard-Jones molecules, Phys. Rev. 159 (1967) 98–103.
[17] M.P. Allen, D.J. Tildesley, Computer Simulation of Liquids, Clarendon Press, Oxford, 1987.
[18] A. Colagrossi, M. Landrini, Numerical simulation of interfacial flows by smoothed particle hydrodynamics, J. Comput. Phys. 191 (2003) 448–475.
[19] K. Shintate, H. Sekine, Numerical simulation of hypervelocity impacts of a projectile on laminated composite plate targets by means of improved SPH method, Compos. Part A: Appl. Sci. Manufact. 35 (2004) 683–692.
[20] L.D. Libersky, A.G. Petschek, T.C. Carney, J.R. Hipp, F.A. Allahdadi, High strain Lagrangian hydrodynamics: a three-dimensional SPH code for dynamic material response, J. Comput. Phys. 109 (1993) 67–75.
[21] J.P. Vila, A. Rompteaux, Calcul du tossage avec Smart Fluids un code de calcul particulaire compressible, in: Proceedings des 7emes Journées de l'Hydrodynamique, 1999.
[22] J. Bonet, S. Kulasegaram, M. Rodriguez-Paz, M. Profit, Variational formulation for the smooth particle hydrodynamics (SPH) simulation of fluid and solid problems, Comput. Meth. Appl. Mech. Eng. 193 (2004) 1245–1256.
[23] S. Muzaferija, M. Peric, P. Sames, T. Schellin, A two-fluid Navier–Stokes solver to simulate water entry, in: 22nd Symposium on Naval Hydrodynamics, The National Academy of Sciences, 2000, pp. 638–649.